Politechnika Warszawska

Warsaw University of Technology

https://repo.pw.edu.pl

Publikacja / Publication	Defect-engineered graphene-on-silicon-carbide platform for magnetic field sensing at greatly elevated temperatures
Autorzy / authors	Ciuk Tymoteusz, Kozłowski Roman, Romanowska Agata, Zagojski Andrzej, Piętak-Jurczak Karolina, Stańczyk Beata, Przyborowska Krystyna, Czołak Dariusz, Kamiński Paweł
DOI wersji wydawcy / Published version DOI	http://dx.doi.org/10.1016/j.cartre.2023.100303
Adres publikacji w Repozytorium URL / Publication address in Repository	https://repo.pw.edu.pl/info/article/WUT062c4c5f40e74f349462b3c8975cd950/
Data opublikowania w Repozytorium / Deposited in Repository on	2024-01-31
Rodzaj licencji / Type of licence	Uznanie Autorstwa - Użycie Niekomercyjne - Bez utworów zależnych 4.0 (CC-BY-NC-ND 4.0) / Attribution-NonCommercial-NoDerivatives (CC BY-NC -ND 4.0)
Wersja dokumentu / Document version	wersja wydawcy / publisher version
Cytuj tę wersję / Cite this version	Ciuk T., Kozłowski R., Romanowska A., Zagojski A., Piętak-Jurczak K., Stańczyk B., Przyborowska K., Czołak D., i Kamiński P., Defect-engineered graphene-on-silicon-carbide platform for magnetic field sensing at greatly elevated temperatures, „Carbon Trends”, 2023, t.13.

Carbon Trends 13 (2023) 100303

Contents lists available at ScienceDirect

Carbon Trends

journal homepage: www.elsevier.com/locate/cartre

Defect-engineered graphene-on-silicon-carbide platform for magnetic field sensing at greatly elevated temperatures

Tymoteusz Ciuk [a,*], Roman Kozłowski [a], Agata Romanowska [a], Andrzej Zagojski [a], Karolina Piętak-Jurczak [a,b], Beata Stańczyk [a], Krystyna Przyborowska [a], Dariusz Czołak [a], Paweł Kamiński [a]

[a] *Łukasiewicz Research Network - Institute of Microelectronics and Photonics, Al. Lotników 32/46, Warsaw, 02-668, Poland*
[b] *Warsaw University of Technology, Faculty of Chemistry, ul. Noakowskiego 3, 00-664, Warsaw, Poland*

ARTICLE INFO

Keywords:
Graphene
Epitaxy
CVD
Ion implantation
Defect levels
HRPITS
Transport properties
Hall effect
Sensor

ABSTRACT

High-temperature electrical properties of p-type hydrogen-intercalated quasi-free-standing epitaxial Chemical Vapor Deposition graphene on semi-insulating vanadium-compensated on-axis 6H-SiC(0001) and high-purity on-axis 4H-SiC(0001) originate from the double-carrier system of spontaneous-polarization-induced holes in graphene and thermally-activated electrons in the substrate. In this study, we pre-epitaxially modify SiC by implanting hydrogen (H^+) and helium (He^+) ions with energies ranging from 20 keV to 50 keV to reconstruct its post-epitaxial defect structure and suppress the thermally-developed electron channel. Through a combination of dark current measurements and High-Resolution Photo-Induced Transient Spectroscopy between 300 K and 700 K, we monitor the impact of ion bombardment on the transport properties of SiC and reveal activation energies of the individual deep-level defects. We find that the ion implantation has a negligible effect on 6H-SiC. Yet in 4H-SiC, it shifts the Fermi level from ~600 meV to ~800 meV below the minimum of the conduction band and reduces the electron concentration by two orders of magnitude. Specifically, it eliminates deep electron traps related to silicon vacancies in the charge state (2-/-) occupying the *h* and *k* sites of the 4H-SiC lattice. Finally, we directly implement the protocol of deep-level defect engineering in the technology of amorphous-aluminum-oxide-passivated Hall effect sensors and introduce a mature sensory platform with record-linear current-mode sensitivity of approximately 80 V/AT with -0.03-%/K stability in a broad temperature range between 300 K and 770 K, and likely far beyond 770 K.

1. Introduction

Transfer-free p-type hydrogen-intercalated [1–5] quasi-free-standing (QFS) epitaxial Chemical Vapor Deposition [6] (CVD) graphene on semi-insulating (SI) vanadium-compensated nominally on-axis 6H-SiC(0001) [7–9] and SI high-purity (HP) nominally on-axis 4H-SiC(0001) [10] has been verified as a high-sensitivity platform, suitable for magnetic field detection at significantly elevated temperatures, as high as 770 K [11,12], and under neutron radiation [13,14]. It is a likely alternative to thin-film active layers based on bismuth [15–18], antimony [19,17], chromium [17], ceramic-chromium [20], gold [21,17], molybdenum [17], tantalum [17], copper [17], NiFe [22,23], InSb [24–28], AlGaN/GaN [29–31], and La-Sr-Mn-O [32].

Unfortunately, the electrical properties of QFS graphene on SI 6H-SiC(0001):V and SI HP 4H-SiC(0001) are stable up to only ~573 K, at which point the single-carrier conductivity governed by spontaneous-polarization-induced holes in graphene evolves into a double-carrier conductivity that involves holes in graphene and thermally-activated electrons in the SiC substrate [11,12] (schematic in Fig. 1). Thermal progression of the SiC-related electron channel was quantified through dark Hall effect measurements. Based on the assumption that the emission of electrons follows the Arrhenius exponent $e^{\frac{-(E_C-E_F)}{k_BT}}$ where $(E_C - E_F)$ is the Fermi level position below the conduction band minimum E_C, k_B is the Boltzmann constant, and T is the absolute temperature, its dominant origin was confronted with literature and tentatively

---

* Corresponding author.
E-mail address: tymoteusz.ciuk@imif.lukasiewicz.gov.pl (T. Ciuk).

https://doi.org/10.1016/j.cartre.2023.100303
Received 24 July 2023; Received in revised form 6 October 2023; Accepted 9 October 2023

Available online 13 October 2023
2667-0569/© 2023 The Author(s). Published by Elsevier Ltd. This is an open access article under the CC BY-NC-ND license (http://creativecommons.org/licenses/by-nc-nd/4.0/).

Pobrano z / Downloaded from Repository of Warsaw University of Technology 2025-09-24 11:16

Pobrano z / Downloaded from Repository of Warsaw University of Technology 2025-09-24 11:16

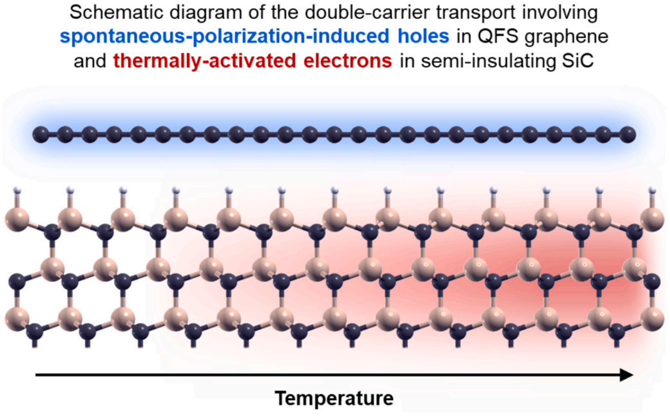

Fig. 1. Conceptual diagram of the thermally-activated double-carrier conductivity at the interface between p-type QFS graphene and hydrogen-saturated semi-insulating on-axis SiC(0001).

ascribed to a deep acceptor level of vanadium in the hexagonal (*h*) site of the SI 6H-SiC:V substrate [11], or to a deep acceptor level related to silicon vacancy $V_{Si}^{2-/-}$ occupying the cubic (*k*) site of the SI HP 4H-SiC lattice [12]. This observation led us to conclude that high-temperature electric charge transport at the interface between QFS graphene and SI SiC depends on the SiC defect structure; hence, its thermal stability could improve if one intentionally suppressed the build-up of the substrate-bound electron channel.

In this study, we experimentally verify the *pre-epitaxial* modification of SI SiC substrates by implanting hydrogen (H^+) and helium (He^+) ions to purposely modify the *post-epitaxial* defect structure of SI SiC and mitigate the thermal transition from the single-carrier to the double-carrier transport. The effect of implantation, followed by the heat exposure associated with graphene CVD epitaxy, is monitored through a temperature-dependent (300 K to 700 K) survey of dark current within the SI SiC substrate, as well as through a detailed analysis and identification of deep traps by High-Resolution Photo-Induced Transient Spectroscopy (HRPITS) [33–35]. The dark current characterization aims to assess the Fermi level position ($E_C - E_F$) and to estimate the bulk electron concentration n and resistivity ρ at the near-surface region of the substrates. The HRPITS addresses the identification of those deep-level defects that can be thermally activated at temperatures between 300 K and 700 K and contribute to the electron build-up at the graphene-SI SiC interface.

The impact of the modification is analyzed separately for SI 6H-SiC:V and SI HP 4H-SiC. Conclusions are drawn, and the ion modification is directly implemented in the technology of high-temperature amorphous-aluminum-oxide-passivated (a-Al_2O_3) Hall effect sensors manufactured on SI HP 4H-SiC(0001) [12]. The sensors have their current-mode sensitivity and mobility assessed as a function of temperature between 300 K and 770 K and compared with the referential unmodified technology reproduced from Ref. [12]. Thus, the titular deep-level defect-engineered graphene-on-SiC platform for high-temperature magnetic field sensing is introduced.

2. Experimental details

2.1. Pre-epitaxial modification of SI SiC substrates with ion implantation

For the experiment, five 10-mm × 10-mm samples were diced from a 4-in 500-µm-thick SI 6H-SiC:V wafer purchased at II-VI Inc., and five 10-mm × 10-mm from a 4-in 500-µm-thick SI HP 4H-SiC wafer supplied by Wolfspeed Inc. One SI 6H-SiC:V and one SI HP 4H-SiC sample served as a reference and were not pre-epitaxially modified. The other eight, with their (0001) surface in as-purchased epi-ready condition, were subject to room-temperature (RT) hydrogen (H^+) and helium (He^+) ions implantation at a fixed dose of 1×10^{14} cm^{-2} and energies in the range of tens of keV. The expected penetration depths (d) assessed with the Stopping and Range of Ions in Matter program (SRIM) varied between $d = 154$ nm and $d = 263$ nm. The conditions of the implantation experiment aimed to possibly equalize the expected penetration depths for the two considered ions. Hence, 20 keV ($d = 156$ nm) and 40 keV ($d = 259$ nm) in the case of H^+, and 25 keV ($d = 154$ nm) and 50 keV ($d = 263$ nm) in the case of He^+. Details of the substrate modifications are summarized in Table 1.

Table 1
Summary of conditions for the pre-epitaxial room-temperature SI SiC substrates modification by ion implantation.

Semi-insulating vanadium-compensated 6H-SiC(0001)

Sample	Ion	Dose [cm^{-2}]	Energy [keV]	Exp. range [nm]
Reference	×	×	×	×
1	H^+	1×10^{14}	20	156
2	H^+	1×10^{14}	40	259
3	He^+	1×10^{14}	25	154
4	He^+	1×10^{14}	50	263

Semi-insulating high-purity 4H-SiC(0001)

Sample	Ion	Dose [cm^{-2}]	Energy [keV]	Exp. range [nm]
Reference	×	×	×	×
1	H^+	1×10^{14}	20	156
2	H^+	1×10^{14}	40	259
3	He^+	1×10^{14}	25	154
4	He^+	1×10^{14}	50	263

2.2. Graphene epitaxy through Chemical Vapor Deposition

Each of the two reference samples (one SI 6H-SiC:V and one SI HP 4H-SiC), as well as the eight pre-epitaxially ion-implanted ones, had in-situ hydrogen-intercalated [5] quasi-free-standing (QFS) graphene (branded GET$^{®}$[36]) grown on them in a hot-wall Aixtron VP508 reactor using the epitaxial Chemical Vapor Deposition (CVD) method in argon flow at 1600 °C [6] and thermally decomposed propane as a source of carbon. The flow of argon was adjusted to create optimum conditions to form a boundary layer that simultaneously inhibits the sublimation [37–40] of the top-most silicon atoms from the SiC(0001) surface and enables mass transport of propane. The deposition was preceded with in-situ etching of the SiC(0001) surface in a purely hydrogen atmosphere at 1600 °C and chamber pressure of 100 mbar, and followed by in-situ hydrogen intercalation at 1000 °C under 900-mbar argon atmosphere.

Directly after the deposition process, graphene RT transport properties were monitored at $I = 1$ mA with a 0.55-T Ecopia HMS-3000 direct-current Hall effect measurement system to verify whether the charge carrier type and sheet concentration was consistent with the theoretically postulated [41–43] $p_s^{6H} \approx 7.5\times10^{12}$ cm^{-2} and $p_s^{4H} \approx 1.2\times10^{13}$ cm^{-2} and whether the charge carrier mobility was comparable with the one expected for conventional processes on unmodified substrates [44–46].

2.3. Test samples preparation and electrical characterization

Once their charge carrier concentration and mobility were measured, all ten samples had the graphene layer fully etched away in oxygen plasma so that bare SI 6H-SiC(0001):V and SI HP 4H-SiC(0001) surfaces remained. Then, onto these surfaces, square-shaped co-planar 2.5-mm × 2.5-mm Ti/Au (10 nm/90 nm) contacts were electron-beam-evaporated, with an inter-distance of 0.7 mm. The samples were diced into rectangular 4-mm × 7-mm chips, each containing a pair of electrodes separated by the 0.7-mm exposed SI SiC channel. As a result, the samples for the electrical characterization took the form of 4-mm × 7-mm × 500-µm slabs.

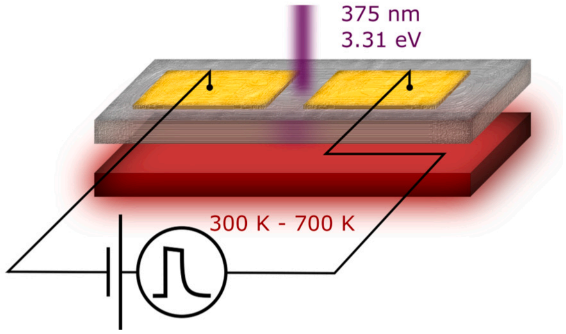

Fig. 2. Schematic of the broad-temperature (300 K to 700 K) experimental setup for the characterization of dark current and the photo-induced current transients. The 4-mm × 7-mm × 500-µm SiC(0001) sample with two co-planar contacts is polarized with a constant voltage bias and periodically illuminated with a 375-nm (3.31-eV) laser.

Dark current (I_{dark}) and HRPITS characterization of the chips were conducted in a vacuum thermal chamber equipped with a LakeShore 331 temperature controller (300 K to 700 K with a step of 10 K). Fixed 20-V inter-electrode voltage bias was applied with a Keithley 2410 SourceMeter. Measured current values were fed into a Keithley 428 current amplifier and further into a computer as a function of the temperature, voltage bias, and laser power control settings. A 15-mW Power Technology semiconductor laser with a beam wavelength of 375 nm was used to provide 3.31-eV photons. The photon flux was regulated with the aid of filters. The absorption coefficient α for 6H-SiC is ~530 cm^{-1} at room temperature and ~2000 cm^{-1} at 700 K [47,48]. The associated penetration depths δ_p are 19 µm and 5 µm, respectively. The absorption coefficient for 4H-SiC is ~25 cm^{-1} at room temperature and ~280 cm^{-1} at 700 K [47,48]. The associated penetration depths are 400 µm and 36 µm, respectively. In all the cases, the penetration depths significantly exceeded the expected sub-micron ion penetration range.

It was assumed that the effective density of states in the SiC conduction band is given by $N_C = 1.73\times10^{15}T^{3/2}$ cm^{-3} for 6H-SiC and $N_C = 3.25\times10^{15}T^{3/2}$ cm^{-3} for 4H-SiC and the bulk electron concentration $n = N_C e^{\frac{-E_A}{k_B T}}$, where E_A is the conductivity activation energy representing the Fermi level position ($E_C - E_F$). Therefore, the measured I_{dark} is proportional to $T^{3/2}e^{\frac{-E_A}{k_B T}}$. Correspondingly, it was expected that the resistivity $\rho = (en\mu_n)^{-1}$, where e is the unit charge, the low-electric-field Caughey-Thomas [49] electron mobility μ_n equals 415 cm^2/Vs in SI 6H-SiC [50], and 947 cm^2/Vs in SI 4H-SiC [50], and both decline with temperature T by a factor $\left(\frac{T}{300\ K}\right)^{\gamma}$ (γ = -2.5 for 6H-SiC [51] and γ = -2.4 for 4H-SiC [51]) due to lattice scattering.

In the HRPITS method, the excess charge carriers were generated by illuminating the gap between the two contacts with 9.7 × 10^{16}-cm^{-2}s^{-1} fluxes of 375-nm (3.31-eV) photons, all lasting for 10 ms and repeated each 500 ms. The photo-current was amplified with a 12-bit amplitude resolution and 1-µs temporal resolution and averaged 250 times to improve the signal-to-noise ratio. For a subsequent data analysis resulting in the calculation of spectral maps, photo-current relaxation waveforms were retrieved from the photo-current transients using the advanced numerical procedures described by Kamiński et al. [34,35]. Each relaxation waveform was normalized to its amplitude at the end of the pulse. Fig. 2 depicts the schematic of the characterization setup. The photo-induced current transients measurements were performed in the temperature range between 300 K and 700 K with a 5-K step.

VESTA software [52] was used to build an auxiliary graphical model and visualize the defects. Necessary structural parameters, i.e., the coordinates, were assumed based on the Crystallography Open Database data [53–61] with lattice constants from a book chapter by Goldberg et al. [62]

The design of the test device, although determined by the HRPITS apparatus, was conceptually convergent with the *van der Pauw* Hall effect structures that had historically helped describe the thermal activation of the double-carrier transport in QFS graphene on SI 6H-SiC:V [11] and SI HP 4H-SiC [12]. In these works, the cross-shaped [46] QFS graphene mesas had also been removed by etching in oxygen plasma, leaving bare SI SiC(0001) substrate between the contacts. The conceptual convergence lets us believe that the conclusions of this section are to be directly implementable in the Hall effect sensor technology.

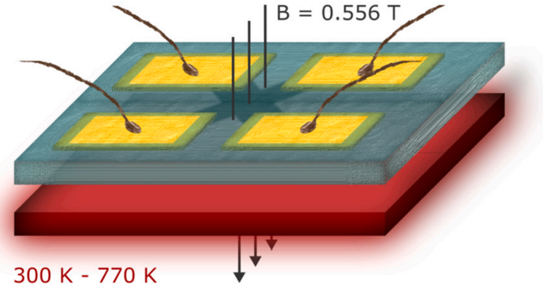

Fig. 3. Schematic of the amorphous-aluminum-oxide-passivated graphene-on-SiC Hall effect sensor operating between 300 K and 770 K.

2.4. Implementation in the Hall effect sensor technology

The pre-epitaxial ion modification was implemented in the technology of 1.4-mm × 1.4-mm Hall effect sensors, manufactured in the number of 96 out of each SI SiC substrate in the 20-mm × 20-mm standard, as previously introduced in Ref. [63]. Through a series of optical lithography-based steps involving metal electron-beam deposition, oxygen plasma etching and atomic layer deposition, the substrates were turned into *van der Pauw* structures, each featuring a cross-shaped [46] 100-µm × 300-µm QFS graphene mesa, Ti/Au (10 nm/90 nm) ohmic contacts, and a 100-nm-thick a-Al$_2$O$_3$ passivation synthesized from trimethylaluminum (TMA) and deionized water at 770 K in a Picosun R200 Advanced ALD reactor [64]. Individual sensors were mounted onto and bonded to in-house-made 6.6-mm × 6.6-mm sapphire holders equipped with four Ti/Au (10 nm/190 nm) corner contacts enabling electrical characterization at I = 1 mA in a 0.556-T direct-current Ecopia AHT55T5 automated Hall effect measurement system between 300 K and 770 K. Schematic of the Hall effect sensor is depicted in Fig. 3, while its real-life implementation evoked in the results and discussion section.

3. Experimental results and discussion

3.1. Transport properties of QFS graphene on the modified SI SiC substrates

The post-growth RT Hall effect characterization of the QFS graphene on pre-epitaxially ion-implanted substrates was performed at I = 1-mA direct current. The measurements revealed that the material is p-type, with the sheet hole concentration p ~10% higher than predicted by theory for unmodified SiC, yet consistent with the reference samples and the statistical data for conventional processes on unmodified SI 6H-SiC:V and SI 4HP 4H-SiC [44,45]. Further supported by hole mobility μ_p of 2000 - 3000 cm^2/Vs, the graphene transport properties implied that the CVD epitaxy followed by in-situ hydrogen intercalation was successful despite the substrate pre-epitaxial modification (Table 2).

3.2. Temperature dependence of dark current in reference and pre-epitaxially ion-implanted SI SiC substrates

For samples polarized with U = 20-V direct bias, the room-temperature dark current I_{dark} was of the order of 1 nA, and up to tens and hundreds of μA at 700 K. Plotted in the form of a natural logarithm of $\frac{I_{dark}}{T^{3/2}}$ as a function of the inverse of $k_B T$, the collective dark current characterization revealed that the pre-epitaxial ion bombardment

Pobrano z / Downloaded from Repository of Warsaw University of Technology 2025-09-24 11:16

Pobrano z / Downloaded from Repository of Warsaw University of Technology 2025-09-24 11:16

Table 2

As-grown room-temperature direct-current Hall-effect-derived transport properties of QFS graphene on reference and pre-epitaxially ion-implanted substrates at $I = 1$ mA.

QFS graphene on SI vanadium-compensated 6H-SiC(0001)

Sample	p [$\times10^{12}$ cm^{-2}]	μ_p [cm^2/Vs]	R_s [Ω/sq]
Reference	8.58	1733	420
H^+: 20 keV	8.17	3304	231
H^+: 40 keV	8.21	3127	242
He^+: 25 keV	8.50	2678	275
He^+: 50 keV	8.18	1389	550

QFS graphene on SI HP 4H-SiC(0001)

Sample	p [$\times10^{13}$ cm^{-2}]	μ_p [cm^2/Vs]	R_s [Ω/sq]
Reference	1.46	666	644
H^+: 20 keV	1.27	2602	189
H^+: 40 keV	1.31	2738	174
He^+: 25 keV	1.31	2305	206
He^+: 50 keV	1.25	2737	183

with H^+ and He^+ ions had hardly any effect on post-epitaxial thermal activation of the electron channel in SI 6H-SiC:V but a significant suppressive effect in SI HP 4H-SiC. The Arrhenius plots of the reference and the modified substrates are illustrated in Fig. 4. The reader is advised to mind that the dark current is plotted as $\frac{I_{dark}}{T^{3/2}}$, which is a decreasing function as long as the I_{dark} remains under the detection threshold of the apparatus (especially visible in Fig. 4 (b)).

In the referential SI 6H-SiC:V substrate, the growth of $\frac{I_{dark}}{T^{3/2}}$ becomes prominent above 380 K, with the conductivity activation energy E_A of 710 meV. Similar temperature thresholds and activation energies are witnessed for the pre-epitaxially ion-implanted samples, namely 719 meV for $H^+{}_{20\text{ keV}}$, 722 meV for $H^+{}_{40\text{ keV}}$, 718 meV for $He^+{}_{25\text{ keV}}$, and 727 meV for the $He^+{}_{50\text{ keV}}$ ions.

In the referential SI HP 4H-SiC sample, the growth of $\frac{I_{dark}}{T^{3/2}}$ becomes prominent above 350 K, with the conductivity activation energy E_A of 615 meV. This time, however, the pre-epitaxially ion-implanted devices prove significantly extended temperature thresholds (approx. 450 K) and increased activation energies, i.e. 820 meV for $H^+{}_{20\text{ keV}}$, 833 meV for $H^+{}_{40\text{ keV}}$, 799 meV for $He^+{}_{25\text{ keV}}$, and 803 meV for the $He^+{}_{50\text{ keV}}$ ions.

Assuming that the bulk electron concentration $n = N_C e^{\frac{-E_A}{k_B T}}$, the ion bombardment only slightly lowered n in SI 6H-SiC:V, yet by nearly two orders of magnitude SI HP 4H-SiC. Correspondingly, the estimated resistivity ρ only moderately increased in SI 6H-SiC:V, yet by almost two orders of magnitude in SI HP 4H-SiC. The extracted activation energies E_A and the related approximate values of n and ρ at 573 K and 700 K are summarized in Table 3. The thermal profiles of n and ρ are plotted in Fig. 5 and Fig. 6, respectively.

The above-presented results indicate that the pre-treatment with H^+ and He^+ ions had barely affected SI 6H-SiC:V. On the other hand, it holds great promise for diminishing the electron concentration in SI HP 4H-SiC and improving the thermal stability of Hall effect sensors.

3.3. *High-resolution photo-induced transient spectroscopy of reference and pre-epitaxially ion-implanted SI SiC substrates*

Recorded photo-current relaxation waveforms related to the thermal emission of charge carriers from deep-level defects were transformed into spectral maps of specific temperature-dependent emission rates e_T with the help of either a correlation procedure or the inverse Laplace transform [65]. An exemplary correlation map is illustrated in Fig. 7 (a). It represents a top view of 3-dimensional folds spanning the temperature T and thermal emission rate e_T axes. Corresponding spectral fringes obtained with inverse Laplace transformation are depicted in Fig. 7 (b). Ridgelines of the fringes (marked as black, solid lines in Fig. 7 (b)) differentiate individual constituents of the collective waveforms, i.e., the desired defect levels. These lines follow the temperature dependence of the charge carrier emission rates for individual defect centers according to the Arrhenius equation [65]:

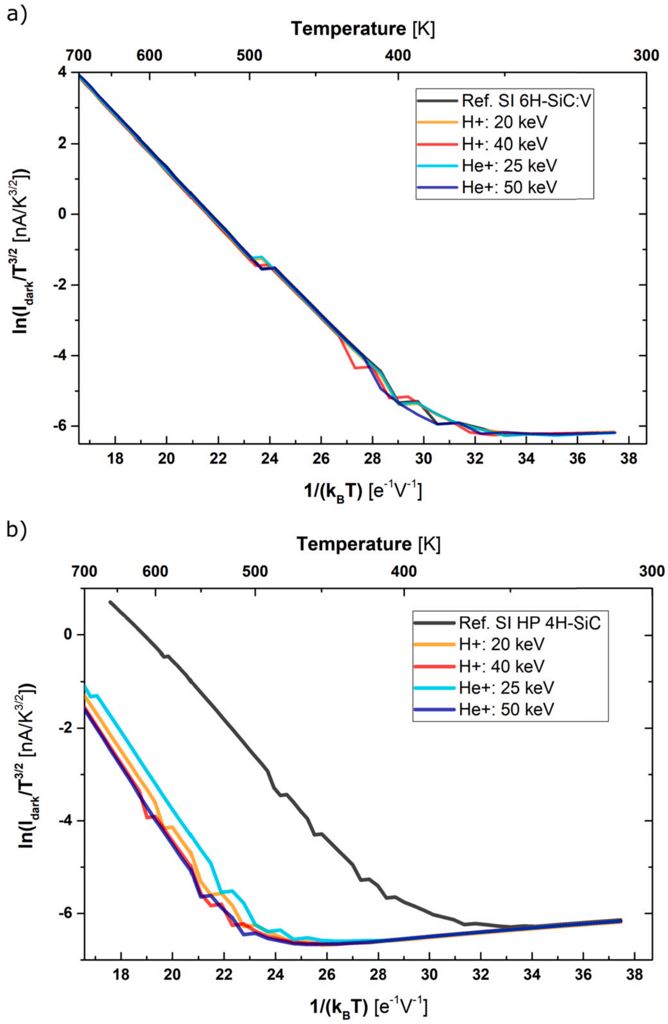

Fig. 4. Natural logarithm of dark current plotted against the inverse of $k_B T$ in the range between 300 K and 700 K measured in reference and pre-epitaxially modified (a) semi-insulating vanadium-compensated on-axis 6H-SiC(0001) and (b) semi-insulating high-purity on-axis 4H-SiC(0001). The modification included bombardment with hydrogen (H^+) and helium (He^+) ions.

$$e_T(T) = AT^2 \exp\left(-\frac{E_a}{k_B T}\right) \tag{1}$$

where k_B is the Boltzmann constant, E_a [eV] describes activation energy of the individual trap, while the pre-exponential factor A [K^{-2}s^{-1}] is a product of the apparent capture cross-section and a material-related constant [34].

Based on both the correlation and the Laplace spectral fringes derived from the photo-current relaxation waveforms recorded in the range of 300 K to 700 K for the reference and the pre-epitaxially ion-implanted samples, the experimentally determined temperature dependencies of the charge carrier emission rates were fitted with the Arrhenius equation to determine the A and E_a parameters and identify the individual defect centers. The centers are tentatively identified by comparing their parameters with the reported electronic properties of point defects in SI SiC [34,35,66]. Obtained values, accompanied by appropriate literature-reported point defect symbols, are summarized in Table 4 (SI 6H-SiC:V) and Table 5 (SI HP 4H-SiC).

In the case of the SI 6H-SiC:V samples, ion implantation did not result in significant changes in the defect structure, except for the trap

Table 3
Dark-current-derived activation energy values in reference and pre-epitaxially ion-implanted SI SiC substrates, based on results shown in Fig. 4 (a) and Fig. 4 (b). The specific bulk electron concentrations n and resistivities ρ are calculated for $T = 573$ K and 700 K.

Semi-insulating vanadium-compensated 6H-SiC(0001)

		573 K		700 K	
Sample	E_A [meV]	n [$\times 10^{13}$ cm^{-3}]	ρ [kΩcm]	n [$\times 10^{14}$ cm^{-3}]	ρ [Ωcm]
Reference	710 ± 6	1.35 ± 0.16	5.63 ± 0.68	2.47 ± 0.24	506 ± 50
H^+: 20 keV	719 ± 6	1.12 ± 0.14	6.77 ± 0.84	2.12 ± 0.21	589 ± 59
H^+: 40 keV	722 ± 7	1.07 ± 0.16	7.09± 1.07	2.05 ± 0.25	611 ± 75
He^+: 25 keV	718 ± 6	1.14 ± 0.14	6.65 ± 0.80	2.16 ± 0.21	580 ± 57
He^+: 50 keV	727 ± 7	0.95 ± 0.13	7.95 ± 1.11	1.86 ± 0.21	671 ± 77

Semi-insulating high-purity 4H-SiC(0001)

		573 K		700 K	
Sample	E_A [meV]	n [$\times 10^{13}$ cm^{-3}]	ρ [kΩcm]	n [$\times 10^{13}$ cm^{-3}]	ρ [Ωcm]
Reference	615 ± 4	17.5 ± 1.53	0.18 ± 0.02	226 ± 16.2	22.3 ± 1.6
H^+: 20 keV	820 ± 16	0.27 ± 0.09	11.4 ± 3.60	7.50 ± 1.93	672 ± 173
H^+: 40 keV	833 ± 15	0.21 ± 0.07	14.8 ± 4.64	6.06 ± 1.55	831 ± 213
He^+: 25 keV	799 ± 12	0.42 ± 0.09	7.39 ± 1.60	10.7 ± 1.90	470 ± 83
He^+: 50 keV	803 ± 14	0.38 ± 0.11	8.10 ± 2.32	9.93 ± 2.33	507 ± 119

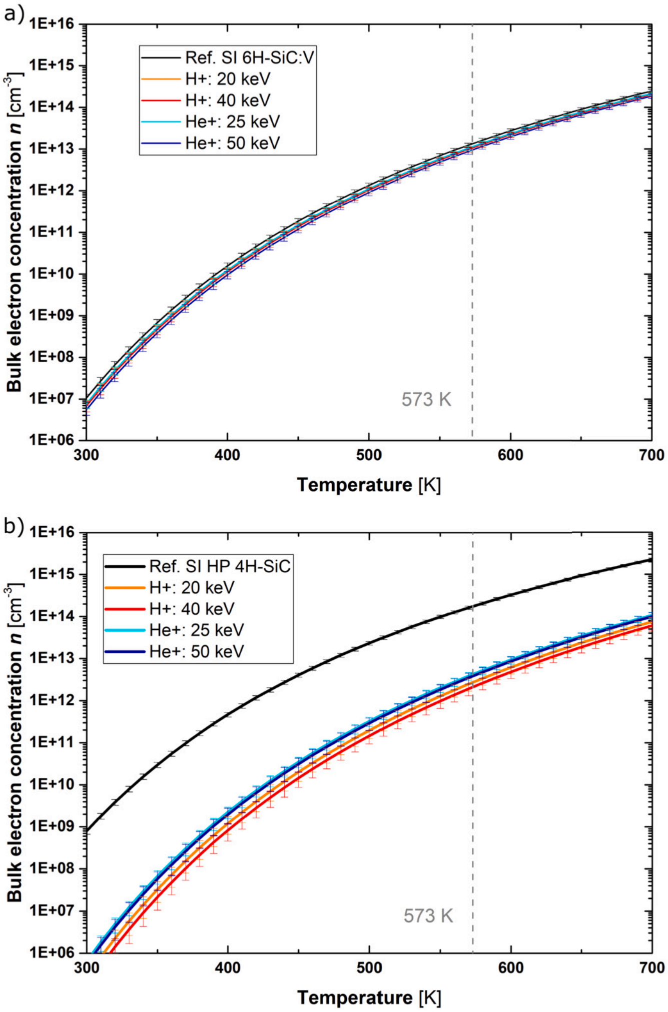

Fig. 5. Estimated thermal changes in bulk electron concentration between 300 K and 700 K in reference and pre-epitaxially modified (a) semi-insulating vanadium-compensated on-axis 6H-SiC(0001) and (b) semi-insulating high-purity on-axis 4H-SiC(0001). The modification included bombardment with hydrogen (H^+) and helium (He^+) ions.

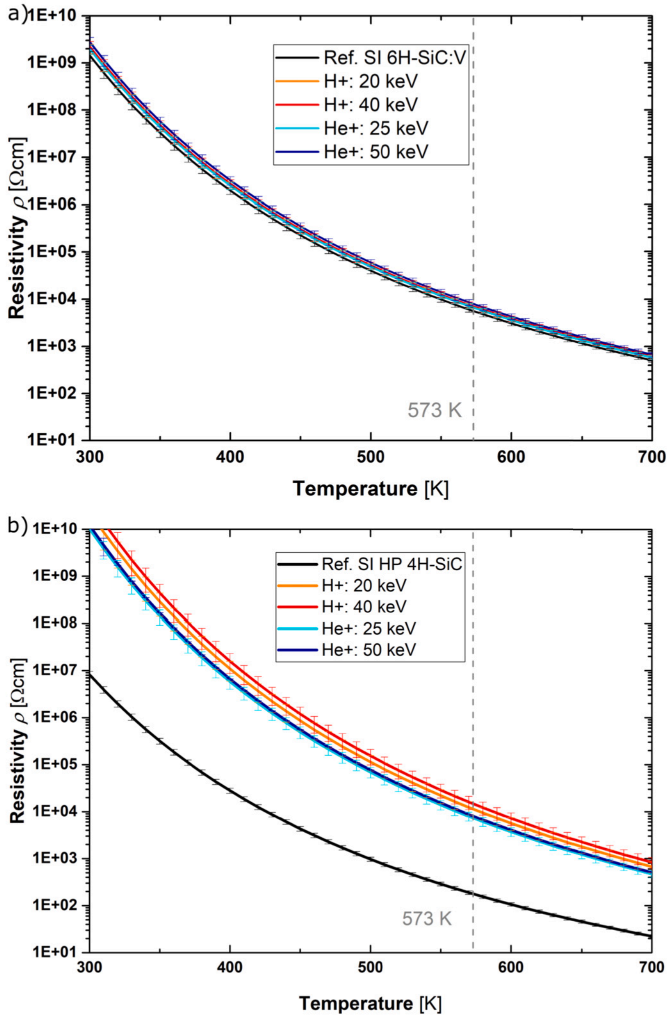

Fig. 6. Estimated thermal changes in resistivity between 300 K and 700 K in reference and pre-epitaxially modified (a) semi-insulating vanadium-compensated on-axis 6H-SiC(0001) and (b) semi-insulating high-purity on-axis 4H-SiC(0001). The modification included bombardment with hydrogen (H^+) and helium (He^+) ions.

Pobrano z / Downloaded from Repository of Warsaw University of Technology 2025-09-24 11:16

Pobrano z / Downloaded from Repository of Warsaw University of Technology 2025-09-24 11:16

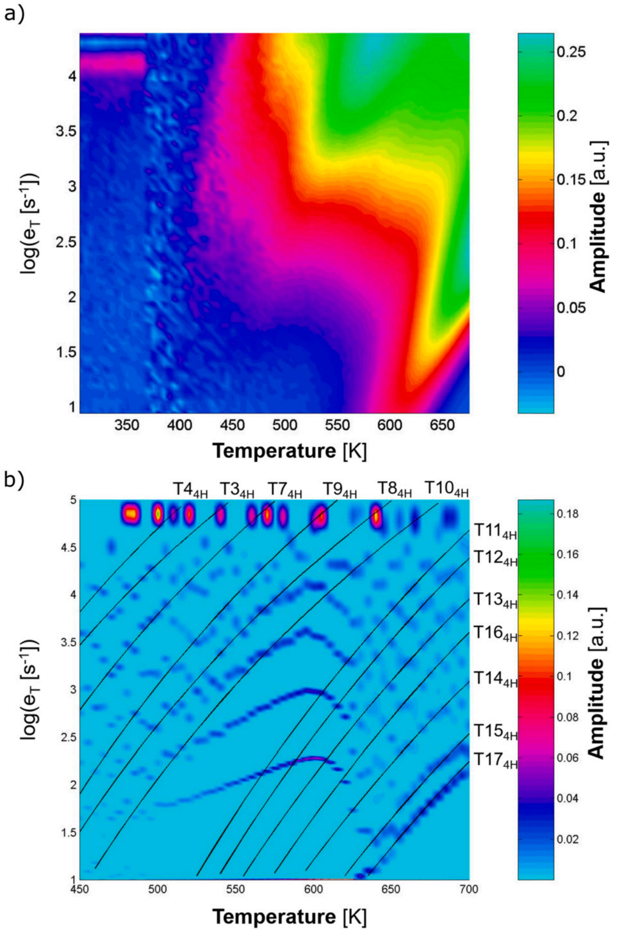

Fig. 7. (a) Spectral map and (b) spectral fringes of the charge carrier emission rate values between 300 K and 700 K for deep-level defects in semi-insulating high-purity on-axis 4H-SiC, pre-epitaxially modified through $H^+{}_{40\ keV}$ bombardment. The map was obtained by means of a two-dimensional analysis of the collective photo-current relaxation waveforms using the correlation procedure. The fringes were calculated by means of a two-dimensional analysis of the collective photo-current relaxation waveforms using the inverse Laplace transform algorithm. The black lines follow the Arrhenius equation describing the emission rate temperature dependencies for the detected centers.

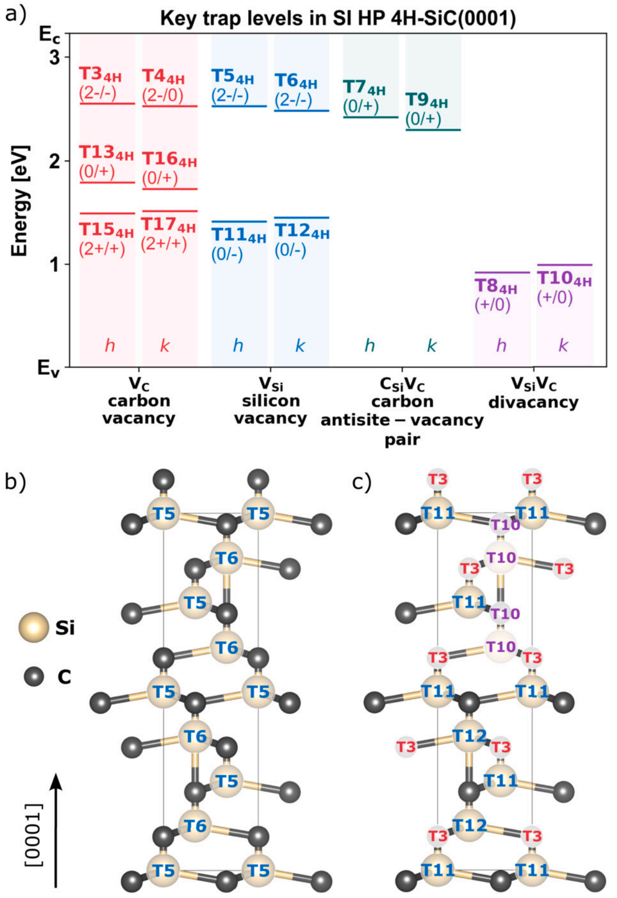

Fig. 8. (a) Schematic visualization of key trap levels detected with High-Resolution Photo-Induced Transient Spectroscopy in semi-insulating high-purity on-axis 4H-SiC. (b) Atomic model illustrating the location of the deep-level defects eliminated by pre-epitaxial bombardment with hydrogen (H^+) ions (labels $T5_{4H}$ and $T6_{4H}$). (c) Corresponding atomic model for the defects eliminated by pre-epitaxial modification with helium (He^+) ions (labels $T3_{4H}$, $T10_{4H}$, $T11_{4H}$, and $T12_{4H}$). The $T5_{4H}$ and $T6_{4H}$ were also eliminated but not displayed for better readability.

labeled $T1_{6H}$. This trap, observed only for the $He^+{}_{25\ keV}$ sample, may be associated with an interstitial defect [67]. The following three detected traps, $T2_{6H}$, $T3_{6H}$, and $T4_{6H}$, are likely to be attributed to electron traps related to vanadium acceptors located at the h and *k* lattice sites, respectively [34]. These defects were observed in all 6H-SiC samples, with no effect of the ion implantation on their characteristics. The differences between the activation energies of the $T5_{6H}$, $T6_{6H}$, and $T7_{6H}$ traps are minor and were detected only by the analysis involving the inverse Laplace transform. The scale of differences and the fact that they remain in the range of 1320 meV - 1400 meV allow us to assign them to hole traps attributed to vanadium donors located at the *h*, k_1, and k_2 sites, respectively [35,66]. The $T8_{6H}$ trap poses identification difficulty on the grounds of the available literature. Finally, the $T9_{6H}$ trap is likely a vanadium donor-related complex defect [67]. It should be added that traps $T8_{6H}$ and $T9_{6H}$ were not detected in the $He^+{}_{50\ keV}$ sample.

As evidenced by the above-presented results, the ion implantation evoked changes in the SI HP 4H-SiC defect structure. The electron trap labeled $T1_{4H}$ can be assigned to a hole trap related to a boron acceptor [69], a residual unintentional impurity. The $T2_{4H}$ might be an electron trap, previously described as EH1 by deep-level capacitance spectroscopy [70]. Both $T1_{4H}$ and $T2_{4H}$ defects were only detected in the reference sample. The $T3_{4H}$ and $T4_{4H}$ traps have parameters consistent with those reported for Z_1 or $Z_{1/2}$ centers. They are likely to be attributed to electron traps related to carbon vacancy acceptors in the (2-/-) and (2-/0) charge states located at the *h* and *k* lattice sites, respectively [73]. The $T3_{4H}$ defect was not observed in He-implanted samples.

The $T5_{4H}$ and $T6_{4H}$ traps are likely electron traps related to silicon vacancy acceptors in the (2-/-) charge states at the *h* and *k* lattice sites, respectively [72]. In turn, the $T7_{4H}$ and $T9_{4H}$ traps can be assigned to an electron trap related to the carbon antisite-vacancy pair ($C_{Si}V_C$) donors in (0/+) charge state located at the two of four lattice sites combinations, namely *hh*, *kh*, *kk*, and *hk* [71,74]. The $T8_{4H}$ and $T10_{4H}$ are likely hole traps identified with the divacancy ($V_{Si}V_C$) donors in the (+/0) charge states located at the two of the four *hh*, *kh*, *kk*, *hk* lattice sites combinations for the constituents [71,74]. The $T11_{4H}$ and $T12_{4H}$ are likely hole traps attributed to the silicon vacancy acceptors in the (-/0) charge states at the *h* and *k* lattice sites, respectively. On the other hand, the 13_{4H} and 16_{4H} traps are likely to be identified with electron traps related to carbon vacancy donors in the (+/0) charge states located at the *h* and *k* sites, respectively [71]. We do not identify the $T14_{6H}$ trap. Finally, traps $T15_{4H}$ and $T17_{4H}$ are likely associated with hole traps related to carbon vacancy in the charge state (2+/+) located at sites *h* and *k*, respectively [71,74]. The measured defect structure, along with the proposed identification, is graphically summarized in Fig. 8.

Pobrano z / Downloaded from Repository of Warsaw University of Technology 2025-09-24 11:16

Table 4
Summary of deep-level defects in SI 6H-SiC:V determined by HRPITS and their tentative literature-based identification.

Semi-insulating vanadium-compensated 6H-SiC

Trap		Sample label					Proposed Identification
		Reference	H$^+$: 20 keV	H$^+$: 40 keV	He$^+$: 25 keV	He$^+$: 50 keV	
T1$_{6H}$	E$_a$ [meV]	-	-	-	525	-	interstitial defect, [67]
	A $\left[K^{-2}s^{-1}\right]$	-	-	-	1.00·10^6	-	
T2$_{6H}$	E$_a$ [meV]	795	750	750	750	750	electron trap, vanadium acceptor at *h* site, [34]
	A $\left[K^{-2}s^{-1}\right]$	6.40·10^6	1.87·10^6	1.87·10^6	1.87·10^6	1.87·10^6	
T3$_{6H}$	E$_a$ [meV]	800	802	802	802	802	electron trap, vanadium acceptor at k_1 site, [34]
	A $\left[K^{-2}s^{-1}\right]$	2.80·10^7	1.92·10^7	1.92·10^7	1.92·10^7	1.92·10^7	
T4$_{6H}$	E$_a$ [meV]	848	848	848	848	848	electron trap, vanadium acceptor at k_2 site, [34]
	A $\left[K^{-2}s^{-1}\right]$	3.52·10^8	3.52·10^8	3.52·10^8	3.52·10^8	3.52·10^8	
T5$_{6H}$	E$_a$ [meV]	1323	1323	1323	1323	1323	hole trap, vanadium donor at *h* site, [68]
	A $\left[K^{-2}s^{-1}\right]$	2.57·10^7	2.57·10^7	2.57·10^7	2.57·10^7	2.57·10^7	
T6$_{6H}$	E$_a$ [meV]	1337	1337	1337	1337	1337	hole trap, vanadium donor at k_1 site
	A $\left[K^{-2}s^{V}-1\right]$	5.80·10^7	5.80·10^7	5.80·10^7	5.80·10^7	5.80·10^7	
T7$_{6H}$	E$_a$ [meV]	1395	1395	1395	1395	1395	hole trap, vanadium donor at k_2 site
	A $\left[K^{-2}s^{-1}\right]$	5.18·10^7	5.18·10^7	5.18·10^7	5.18·10^7	5.18·10^7	
T8$_{6H}$	E$_a$ [meV]	1435	1435	1435	1435	-	unidentified defect
	A $\left[K^{-2}s^{-1}\right]$	3.16·10^6	3.16·10^6	3.16·10^6	3.16·10^6	-	
T9$_{6H}$	E$_a$ [meV]	1704	1704	1704	1704	-	vanadium donor-related complex, [68]
	A $\left[K^{-2}s^{-1}\right]$	6.16·10^7	6.16·10^7	6.16·10^7	6.16·10^7	-	

Table 5
Summary of deep-level defects in SI HP 4H-SiC determined by HRPITS and their tentative literature-based identification.

Semi-insulating high-purity 4H-SiC

Trap		Sample label					Proposed Identification
		Reference	H$^+$: 20 keV	H$^+$: 40 keV	He$^+$: 25 keV	He$^+$: 50 keV	
T1$_{4H}$	E$_a$ [meV],	335	-	-	-	-	hole trap, boron acceptor, [69]
	A $\left[K^{-2}s^{-1}\right]$	4.75·10^4	-	-	-	-	
T2$_{4H}$	E$_a$ [meV]	474	-	-	-	-	electron trap, EH1, S/S$_1$, [66,70]
	A $\left[K^{-2}s^{-1}\right]$	2.47·10^6	-	-	-	-	
T3$_{4H}$	E$_a$ [meV]	684	684	684	-	-	electron trap, V_C at *h* site, (2-/-), Z$_{1/2}$, [71,34]
	A $\left[K^{-2}s^{-1}\right]$	6.65·10^5	6.65·10^5	6.65·10^5	-	-	
T4$_{4H}$	E$_a$ [meV]	707	707	707	707	707	electron trap, V_C at *k* site, (2-/0), Z$_{1/2}$, [71,34]
	A $\left[K^{-2}s^{-1}\right]$	2.67·10^6	2.67·10^6	2.67·10^6	2.67·10^6	2.67·10^6	
T5$_{4H}$	E$_a$ [meV]	708	-	-	-	-	electron trap, V_{Si} at *h* site, (2-/-), [72,71]
	A $\left[K^{-2}s^{-1}\right]$	1.61·10^8	-	-	-	-	
T6$_{4H}$	E$_a$ [meV]	753	-	-	-	-	electron trap, V_{Si} at *k* site, (2-/-), [72,71]
	A $\left[K^{-2}s^{-1}\right]$	3.32·10^7	-	-	-	-	
T7$_{4H}$	E$_a$ [meV]	816	816	816	816	816	electron trap, $C_{Si}V_C$ at *h* site, (0/+), [71]
	A $\left[K^{-2}s^{-1}\right]$	4.14·10^6	4.14·10^6	4.14·10^6	4.14·10^6	4.14·10^6	
T8$_{4H}$	E$_a$ [meV]	917	917	917	917	917	hole trap, $V_{Si}V_C$ at *h* site, (+/0), [71]
	A $\left[K^{-2}s^{-1}\right]$	2.98·10^6	2.98·10^6	2.98·10^6	2.98·10^6	2.98·10^6	
T9$_{4H}$	E$_a$ [meV]	938	938	938	938	938	electron trap, $C_{Si}V_C$ at *k* site, (0/+), [71]
	A $\left[K^{-2}s^{-1}\right]$	1.28·10^7	1.28·10^7	1.28·10^7	1.28·10^7	1.28·10^7	
T10$_{4H}$	E$_a$ [meV]	986	986	986	-	-	hole trap, $V_{Si}V_C$ at *k* site, (+/0), [71]
	A $\left[K^{-2}s^{-1}\right]$	4.03·10^6	4.03·10^6	4.03·10^6	-	-	
T11$_{4H}$	E$_a$ [meV]	1420	1410	1410	-	-	hole trap, V_{Si} at *k* site, (0/-), [71]
	A $\left[K^{-2}s^{-1}\right]$	2.73·10^9	1.38·10^9	1.38·10^9	-	-	
T12$_{4H}$	E$_a$ [meV]	1450	1450	1450	-	1450	hole trap, V_{Si} at *h* site, (0/-), [71]
	A $\left[K^{-2}s^{-1}\right]$	1.40·10^9	1.40·10^9	1.40·10^9	-	1.40·10^9	
T13$_{4H}$	E$_a$ [meV]	1440	1440	1440	1440	1440	electron trap, V_C at *h* site, (0/+) [71]
	A $\left[K^{-2}s^{-1}\right]$	4.28·10^8	4.28·10^8	4.28·10^8	4.28·10^8	4.28·10^8	
T14$_{4H}$	E$_a$ [meV]	1449	1449	1449	1449	1449	unidentified defect
	A $\left[K^{-2}s^{-1}\right]$	6.66·10^7	6.66·10^7	6.66·10^7	6.66·10^7	6.66·10^7	
T15$_{4H}$	E$_a$ [meV]	1489	1489	1489	1489	1489	hole trap, V_C at *h* site, (2+/+), [71]
	A $\left[K^{-2}s^{-1}\right]$	3.65·10^7	3.65·10^7	3.65·10^7	3.65·10^7	3.65·10^7	
T16$_{4H}$	E$_a$ [meV]	1503	1503	1503	1503	1503	electron trap, V_C at *k* site, (0/+), [71]
	A $\left[K^{-2}s^{-1}\right]$	5.37·10^8	5.37·10^8	5.37·10^8	5.37·10^8	5.37·10^8	
T17$_{4H}$	E$_a$ [meV]	1511	1511	1511	1511	1511	hole trap, V_C at *k* site, (2+/+), [71]
	A $\left[K^{-2}s^{-1}\right]$	2.70·10^7	2.70·10^7	2.70·10^7	2.70·10^7	2.70·10^7	

Pobrano z / Downloaded from Repository of Warsaw University of Technology 2025-09-24 11:16

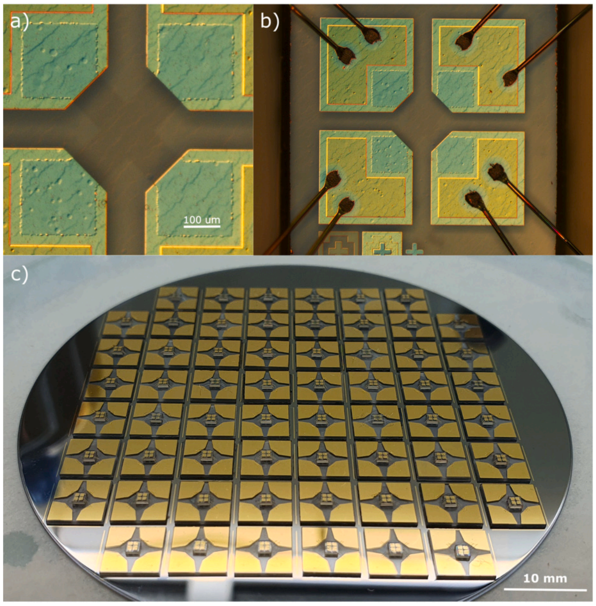

Fig. 9. Nomarski interference contrast optical image of the technology implementation. (a) Close-up of a single structure featuring a cross-shaped 100-µm × 300-µm epitaxial CVD QFS-graphene mesa on SI HP 4H-SiC(0001), all passivated with a 100-nm-thick atomic-layer-deposited amorphous aluminum oxide layer. (b) Individual wire-bonded 1.4-mm × 1.4-mm Hall effect sensor. (c) Batch of Hall effect sensors mounted onto 6.6-mm × 6.6-mm custom-made sapphire holders.

3.4. Verification of the pre-epitaxial ion implantation in the technology of Hall effect sensors

The pre-epitaxial modification with $H^+{}_{20\ \mathrm{keV}}$, $H^+{}_{40\ \mathrm{keV}}$, $He^+{}_{25\ \mathrm{keV}}$, and $He^+{}_{50\ \mathrm{keV}}$ ions was implemented in the technology of a-Al_2O_3-passivated Hall effect sensors. Fig. 9 illustrates successive close-ups of the realization of the platform and exemplary structures awaiting broad-temperature verification between 300 K and 770 K.

For visual clarity, five Hall effect sensors for each modification had their current-mode sensitivity (S_I) and hole mobility profiles plotted against a collection of reference curves reproduced from Ref. [12] representing sensors on unmodified SI HP 4H-SiC(0001). The S_I is defined as the sensor voltage response to the magnetic field:

$$S_I = \frac{\partial U_{Hall}}{\partial B}/I = 1/(pe) \tag{2}$$

where U_{Hall} is the Hall voltage, B is the magnetic field, I is the feed current, p is the hole sheet concentration, and e is the unit charge. Fig. 10 illustrates the effect of the $H^+{}_{20\ \mathrm{keV}}$ and $H^+{}_{40\ \mathrm{keV}}$ implantations on the S_I.

Even though the dark-current characterization and the detailed HRPITS analysis did not bring out a noticeable difference between the effect of $H^+{}_{20\ \mathrm{keV}}$ and $H^+{}_{40\ \mathrm{keV}}$ modification, the two resulted in a substantially miscellaneous performance of the sensors. The $H^+{}_{20\ \mathrm{keV}}$-modified sensors display comparable current-mode sensitivities with regard to the reference ones, while the $H^+{}_{40\ \mathrm{keV}}$-modified structures have their sensitivities lowered and dispersed. Both modifications result in the curves being more linear yet downward inclined. The expected thermal stabilities of S_I defined as:

$$\alpha = \frac{(S_I^{T_2} - S_I^{T_1})}{S_I^{T_1}(T_2 - T_1)} \times 100\% \tag{3}$$

where $T_1 = 300$ K and $T_2 = 770$ K, are α = -0.03%/K for $H^+{}_{20\ \mathrm{keV}}$ and α = -0.06%/K for $H^+{}_{40\ \mathrm{keV}}$. Fundamentally, within the critical sub-range of 700 K to 770 K (Fig. 10 (b)), both modifications eliminated the characteristic bending that is a hallmark of the thermally-activated double-carrier conductivity.

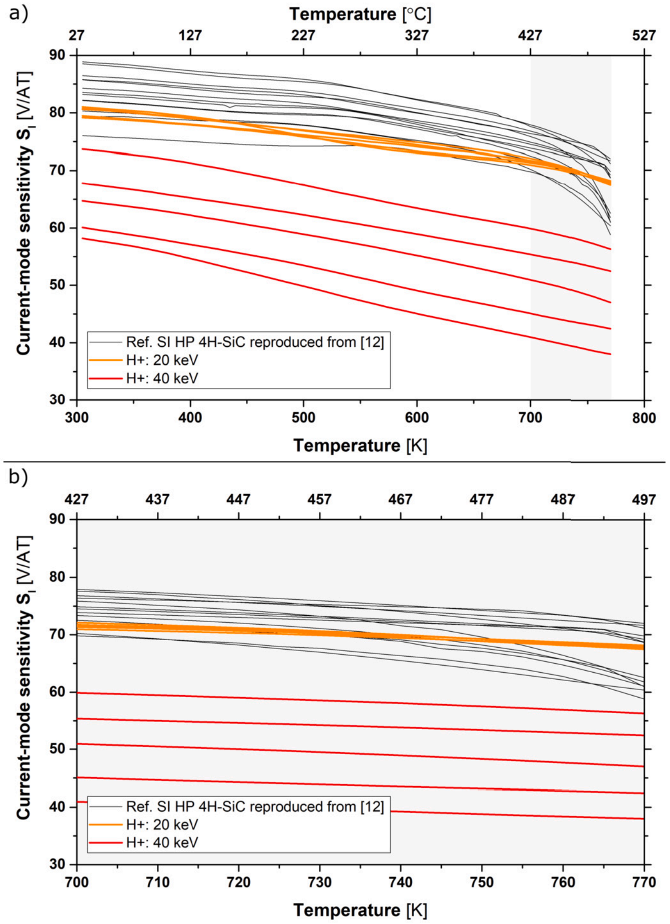

Fig. 10. Representative curves of current-mode sensitivity of Hall effect sensors fabricated on SI HP 4H-SiC(0001), pre-epitaxially modified through $H^+{}_{20\ \mathrm{keV}}$ (orange) and $H^+{}_{40\ \mathrm{keV}}$ (red) bombardment. The curves are plotted against a collection of reference data (black) for unmodified SI HP 4H-SiC(0001) reproduced from Ref. [12]. (a) Full temperature range between 300 K and 770 K. (b) Close-up of the critical sub-range between 700 K and 770 K.

For comparison, sensors on $He^+{}_{25\ \mathrm{keV}}$-modified and $He^+{}_{50\ \mathrm{keV}}$-modified SI HP 4H-SiC(0001) have their S_I curves inclined at a greater angle of -0.06%/K and -0.08%/K, respectively, and nominally lowered versus the unmodified ones. Still, within the critical high-temperature sub-range, both modifications brought the expected elimination of the symptomatic bending (Fig. 11).

The Hall-effect-derived hole mobilities in sensors on hydrogen-modified SI HP 4H-SiC(0001) display a slightly more linear and downward inclined character. Their nominal value remains unaffected by the $H^+{}_{20\ \mathrm{keV}}$ implantation, yet to some extent is deteriorated by the $H^+{}_{40\ \mathrm{keV}}$ modification (Fig. 12 (a)). Sensors in the helium-modified technology have their mobilities steeper and reduced compared with the unmodified ones (Fig. 12 (b)).

It is evident that all the considered pre-epitaxial modifications reconstructed the post-epitaxial defect structure of SI HP 4H-SiC and mitigated the thermal build-up of the detrimental electron channel. Of the two ions, the H^+ serves the sensory platform better than the He^+ ones. Preferably, the energy of the hydrogen ions is lessened to sub-20 keV to meet optimum performance.

Interestingly, the magneto-thermal response of the Hall effect sensors on modified SI HP 4H-SiC is by far more complex and miscellaneous than the detailed High-Resolution Photo-Induced Transient Spectroscopy would suggest. In particular, the HRPITS analysis did not dis-

Pobrano z / Downloaded from Repository of Warsaw University of Technology 2025-09-24 11:16

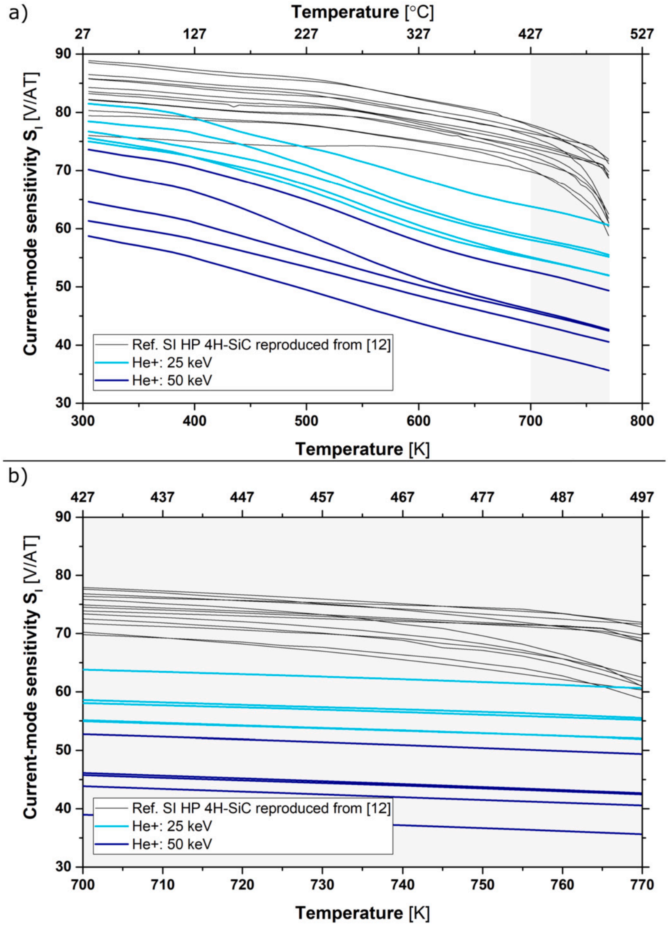

Fig. 11. Representative curves of current-mode sensitivity of Hall effect sensors fabricated on SI HP 4H-SiC(0001), pre-epitaxially modified through $He^+_{25\ keV}$ (cyan) and $He^+_{50\ keV}$ (navy blue) bombardment. The curves are plotted against a collection of reference data (black) for unmodified SI HP 4H-SiC(0001) reproduced from Ref. [12]. (a) Full temperature range between 300 K and 770 K. (b) Close-up of the critical sub-range between 700 K and 770 K.

cern between the $H^+_{20\ keV}$ and $H^+_{40\ keV}$ modifications. Yet, their effect on the current-mode sensitivity and hole mobility curves of the sensors is admittedly different, implying that the *a*-Al$_2$O$_3$/QFS-graphene/4H-SiC could serve to monitor subtle changes in the SI HP 4H-SiC electrical properties.

4. Summary and conclusions

In this report, we have conducted pre-epitaxial room-temperature modification of Si-terminated on-axis semi-insulating vanadium-compensated on-axis 6H-SiC and semi-insulating high-purity on-axis 4H-SiC by implanting a fixed dose of 1×10^{14} cm^{-2} of hydrogen (H^+) or helium (He^+) ions, with energies ranging from 20 keV to 50 keV. Then, the SI 6H-SiC:V and SI HP 4H-SiC underwent graphene Chemical Vapor Deposition epitaxy at 1600 °C, followed by in-situ hydrogen intercalation. Upon subsequent removal of the quasi-free-standing graphene in oxygen plasma, reference and the modified samples had their electrical properties assessed through dark current measurements between 300 K and 700 K.

We found that the ion bombardment had a negligible effect on SI 6H-SiC:V, yet a substantial one on SI HP 4H-SiC. Specifically for SI HP 4H-SiC, the modification brought about a shift of the Fermi level position from ~600 meV to ~800 meV below the minimum of the conduction band, which resulted in an estimated reduction of room-temperature bulk electron concentration from ~1×10^{9} cm^{-3} to ~1×10^{6} cm^{-3}, and an estimated increase in room-temperature resistivity from ~1×10^{7} Ωcm to ~1×10^{10} Ωcm.

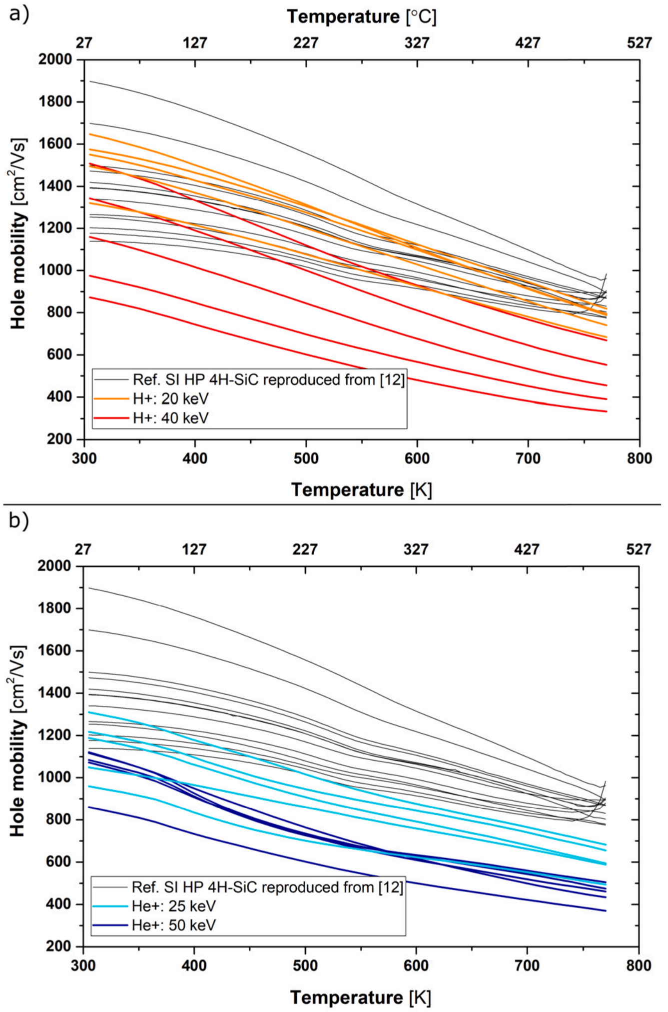

Fig. 12. Representative curves of hole mobility in Hall effect sensors fabricated on SI HP 4H-SiC(0001), pre-epitaxially modified through (a) $H^+_{20\ keV}$ (orange) and $H^+_{40\ keV}$ (red) bombardment, or (b) $He^+_{25\ keV}$ (cyan) and $H^+_{50\ keV}$ (navy blue) bombardment. The curves are plotted against a collection of reference data (black) for unmodified SI HP 4H-SiC(0001) reproduced from Ref. [12].

Details of the defect structure of reference and the pre-epitaxially modified SI SiC were revealed through High-Resolution 375-nm Photo-Induced Transient Spectroscopy, exploiting either a correlation procedure or the inverse Laplace apparatus to transform the collective photo-current relaxation waveforms into spectral maps of specific temperature-dependent emission rates and to discern individual constituents related to the activation energies of the SI SiC deep trap levels.

We identified nine trap levels in SI 6H-SiC:V and seventeen in SI HP 4H-SiC. The choice of the ion type (H^+ or He^+) and energy had a minor effect on the post-epitaxial defect structure of SI HP 4H-SiC. Yet, each modification eliminated deep electron traps related to silicon vacancies in the charge state (2-/-) occupying the *h* and *k* sites of the SI HP 4H-SiC lattice.

Next, we directly implemented the protocol of pre-epitaxial H^+ or He^+ ions implantation in the technology of *a*-Al$_2$O$_3$-passivated Hall effect sensors featuring quasi-free-standing epitaxial Chemical Vapor Deposition graphene on SI HP 4H-SiC(0001). The sensors had their current-mode sensitivity and mobility assessed as a function of temperature between 300 K and 770 K and compared with the referential unmodified technology. Within the critical range of 700 K to 770 K,

Pobrano z / Downloaded from Repository of Warsaw University of Technology 2025-09-24 11:16

all modifications eliminated the characteristic downward bending of the current-mode sensitivity, previously identified as a hallmark of the thermally-activated double-carrier conductivity.

Specifically, the $H^{+}{}_{20\ \mathrm{keV}}$ modification resulted in the Hall effect sensor having record-linear current-mode sensitivity of approximately 80 V/AT with a thermal stability of -0.03%/K in a broad temperature range between 300 K and 770 K. The linearity of the sensitivity curves indicated that the deep-level defect-engineered a-Al_2O_3/QFS-graphene/4H-SiC sensory platform is likely operational far beyond 770 K.

Interestingly, the magneto-thermal response of the a-Al_2O_3/QFS-graphene/4H-SiC system to the pre-epitaxial ion implantation protocol is by far more pronounced than the High-Resolution Photo-Induced Transient Spectroscopy would imply. It suggests that the composition is not only suited for high-temperature magnetic field detection. It could also serve as a high-sensitivity platform to evaluate even subtle changes in the electrical properties of semi-insulating high-purity 4H-SiC.

Declaration of competing interest

The authors declare that they have no known competing financial interests or personal relationships that could have appeared to influence the work reported in this paper.

Data availability

The data that support the findings of this study are available from the corresponding author upon reasonable request.

Acknowledgements

The research leading to these results has received funding from the National Science Centre, Poland, under Grant Agreement No. **OPUS 2019/33/B/ST3/02677** for project *“Influence of the silicon carbide and the dielectric passivation defect structure on high-temperature electrical properties of epitaxial graphene”* and the National Centre for Research and Development, Poland, under Grant Agreement No. **M-ERA.NET3/2021/83/I4BAGS/2022** for project *“Ion Implantation for Innovative Interface modifications in BAttery and Graphene-enabled Systems”*. The **M-ERA.NET3** has received funding from the European Union’s Horizon 2020 research and innovation programme under Grant Agreement No. **958174**.

References

[1] C. Riedl, C. Coletti, T. Iwasaki, A.A. Zakharov, U. Starke, Quasi-free-standing epitaxial graphene on SiC obtained by hydrogen intercalation, Phys. Rev. Lett. 103 (24) (Dec. 2009), https://doi.org/10.1103/physrevlett.103.246804.

[2] S. Watcharinyanon, C. Virojanadara, J. Osiecki, A. Zakharov, R. Yakimova, R. Uhrberg, L. Johansson, Hydrogen intercalation of graphene grown on 6H-SiC(0001), Surf. Sci. 605 (17–18) (2011) 1662–1668, https://doi.org/10.1016/j.susc.2010.12.018.

[3] J.D. Emery, V.D. Wheeler, J.E. Johns, M.E. McBriarty, B. Detlefs, M.C. Hersam, D.K. Gaskill, M.J. Bedzyk, Structural consequences of hydrogen intercalation of epitaxial graphene on SiC(0001), Appl. Phys. Lett. 105 (16) (2014) 161602, https://doi.org/10.1063/1.4899142.

[4] J. Sołtys, J. Piechota, M. Ptasinska, S. Krukowski, Hydrogen intercalation of single and multiple layer graphene synthesized on Si-terminated SiC(0001) surface, J. Appl. Phys. 116 (8) (2014) 083502, https://doi.org/10.1063/1.4893750.

[5] M.J. Szary, S. El-Ahmar, T. Ciuk, The impact of partial h intercalation on the quasi-free-standing properties of graphene on SiC(0001), Appl. Surf. Sci. 541 (2021) 148668, https://doi.org/10.1016/j.apsusc.2020.148668.

[6] W. Strupinski, K. Grodecki, A. Wysmolek, R. Stepniewski, T. Szkopek, P.E. Gaskell, A. Grüneis, D. Haberer, R. Bozek, J. Krupka, J.M. Baranowski, Graphene epitaxy by chemical vapor deposition on SiC, Nano Lett. 11 (4) (2011) 1786–1791, https://doi.org/10.1021/nl200390e.

[7] K. Maier, H.D. Müller, J. Schneider, Transition metals in silicon carbide (SiC): vanadium and titanium, Mater. Sci. Forum 83–87 (1992) 1183–1194, https://doi.org/10.4028/www.scientific.net/msf.83-87.1183.

[8] H.M. Hobgood, R.C. Glass, G. Augustine, R.H. Hopkins, J. Jenny, M. Skowronski, W.C. Mitchel, M. Roth, Semi-insulating 6H–SiC grown by physical vapor transport, Appl. Phys. Lett. 66 (11) (1995) 1364–1366, https://doi.org/10.1063/1.113202.

[9] W.C. Mitchel, W.D. Mitchell, G. Landis, H.E. Smith, W. Lee, M.E. Zvanut, Vanadium donor and acceptor levels in semi-insulating 4H- and 6H-SiC, J. Appl. Phys. 101 (1) (2007) 013707, https://doi.org/10.1063/1.2407263.

[10] M.V.S. Chandrashekhar, I. Chowdhury, P. Kaminski, R. Kozlowski, P.B. Klein, T. Sudarshan, High purity semi-insulating 4H-SiC epitaxial layers by defect-competition epitaxy: controlling Si vacancies, Appl. Phys. Express 5 (2) (2012) 025502, https://doi.org/10.1143/apex.5.025502.

[11] T. Ciuk, A. Kozlowski, P.P. Michalowski, W. Kaszub, M. Kozubal, Z. Rekuc, J. Podgorski, B. Stanczyk, K. Przyborowska, I. Jozwik, A. Kowalik, P. Kaminski, Thermally-activated double-carrier transport in epitaxial graphene on vanadium-compensated 6H-SiC as revealed by Hall effect measurements, Carbon 139 (2018) 776–781, https://doi.org/10.1016/j.carbon.2018.07.049.

[12] T. Ciuk, B. Stanczyk, K. Przyborowska, D. Czolak, A. Dobrowolski, J. Jagiello, W. Kaszub, M. Kozubal, R. Kozlowski, P. Kaminski, High-temperature Hall effect sensor based on epitaxial graphene on high-purity semiinsulating 4H-SiC, IEEE Trans. Electron Devices 66 (7) (2019) 3134–3138, https://doi.org/10.1109/ted.2019.2915632.

[13] S. El-Ahmar, M.J. Szary, T. Ciuk, R. Prokopowicz, A. Dobrowolski, J. Jagiełło, M. Ziemba, Graphene on SiC as a promising platform for magnetic field detection under neutron irradiation, Appl. Surf. Sci. 590 (2022) 152992, https://doi.org/10.1016/j.apsusc.2022.152992.

[14] S. El-Ahmar, M. Przychodnia, J. Jankowski, R. Prokopowicz, M. Ziemba, M.J. Szary, W. Reddig, J. Jagiełło, A. Dobrowolski, T. Ciuk, The comparison of InSb-based thin films and graphene on SiC for magnetic diagnostics under extreme conditions, Sensors 22 (14) (2022) 5258, https://doi.org/10.3390/s22145258.

[15] I. Ďuran, S. Entler, M. Kohout, M. Kočan, G. Vayakis, High magnetic field test of bismuth Hall sensors for ITER steady state magnetic diagnostic, Rev. Sci. Instrum. 87 (11) (2016) 11D446, https://doi.org/10.1016/j.fusengdes.2017.05.142.

[16] I. Ďuran, S. Entler, M. Kočan, M. Kohout, L. Viererbl, R. Mušálek, T. Chráska, G. Vayakis, Development of Bismuth Hall sensors for ITER steady state magnetic diagnostics, Fusion Eng. Des. 123 (2017) 690–694, https://doi.org/10.1016/j.fusengdes.2017.05.142.

[17] S. Entler, I. Duran, K. Kovarik, P. Sladek, O. Grover, M. Vilemova, D. Najman, M. Kohout, J. Sebek, K. Vyborny, Z. Soban, Temperature dependence of the Hall coefficient of sensitive layer materials considered for DEMO Hall sensors, Fusion Eng. Des. 153 (2020) 111454, https://doi.org/10.1016/j.fusengdes.2020.111454.

[18] M. Kocan, I. Duran, S. Entler, G. Vayakis, P. Agostinetti, M. Brombin, J.M. Carmona, G. Gambetta, T. Jirman, N. Marconato, P. Moreau, S. Peruzzo, P. Spuig, M. Walsh, Steady state magnetic sensors for ITER and beyond: development and final design (invited), Rev. Sci. Instrum. 89 (10) (2018) 10J119, https://doi.org/10.1063/1.5038871.

[19] S. Entler, I. Duran, M. Kocan, G. Vayakis, M. Kohout, J. Sebek, P. Sladek, O. Grover, K. Vyborny, Prospects for the steady-state magnetic diagnostic based on antimony Hall sensors for future fusion power reactors, Fusion Eng. Des. 146 (September 2018) (2019) 526–530, https://doi.org/10.1016/j.fusengdes.2019.01.013.

[20] S. Entler, Z. Soban, I. Duran, K. Kovarik, K. Vyborny, J. Sebek, S. Tazlaru, J. Strelecek, P. Sladek, Ceramic-chromium Hall sensors for environments with high temperatures and neutron radiation, Sensors (Switzerland) 21 (3) (2021) 1–12, https://doi.org/10.3390/s21030721.

[21] I. Bolshakova, M. Bulavin, N. Kargin, Y. Kost, T. Kuech, S. Kulikov, M. Radishevskiy, F. Shurygin, M. Strikhanov, I. Vasil’evskii, A. Vasyliev, Metal Hall sensors for the new generation fusion reactors of DEMO scale, Nucl. Fusion 57 (11) (2017) 116042, https://doi.org/10.1088/1741-4326/aa7867.

[22] T. Jeon, J.H. Lee, A. Talantsev, C.G. Kim, Planar Hall resistance sensor with improved thermal stability, IEEE Magn. Lett. 10 (2019) 1–5, https://doi.org/10.1109/lmag.2019.2943054.

[23] M. Mahfoud, Q.-H. Tran, S. Wane, D.-T. Ngo, E.H. Belarbi, A. Boukra, M. Kim, A. Elzwawy, C. Kim, G. Reiss, B. Dieny, A. Bousseksou, F. Terki, Reduced thermal dependence of the sensitivity of a planar Hall sensor, Appl. Phys. Lett. 115 (7) (2019) 072402, https://doi.org/10.1063/1.5110671.

[24] I. Ďuran, M. Oszwaldowski, K. Kovařík, J. Jankowski, S. El-Ahmar, L. Viererbl, Z. Lahodová, Investigation of impact of neutron irradiation on properties of InSb-based Hall plates, J. Nucl. Mater. 417 (1–3) (2011) 846–849, https://doi.org/10.1016/j.jnucmat.2010.12.149.

[25] J. Jankowski, S. El-Ahmar, M. Oszwaldowski, Hall sensors for extreme temperatures, Sensors 11 (1) (2011) 876–885, https://doi.org/10.3390/s110100876.

[26] J. Jankowski, R. Prokopowicz, K. Pytel, S. El-Ahmar, Toward the development of an InSb-based neutron-resistant Hall sensor, IEEE Trans. Nucl. Sci. 66 (6) (2019) 926–931, https://doi.org/10.1109/tns.2019.2912720.

[27] A. Quercia, A. Pironti, I. Bolshakova, R. Holyaka, I. Duran, A. Murari, J. Contributors, Long term operation of the radiation-hard Hall probes system and the path toward a high performance hybrid magnetic field sensor, Nucl. Fusion 62 (10) (2022) 106032, https://doi.org/10.1088/1741-4326/ac8aad.

[28] W. Reddig, M. Przychodnia, T. Ciuk, S. El-Ahmar, High-temperature stability of sensor platforms designed to detect magnetic fields in a harmful radiation environment, IEEE Sens. Lett. 7 (8) (2023) 1–4, https://doi.org/10.1109/lsens.2023.3297795.

[29] S. Koide, H. Takahashi, A. Abderrahmane, I. Shibasaki, A. Sandhu, High temperature Hall sensors using AlGaN/GaN HEMT structures, J. Phys. Conf. Ser. 352 (2012) 012009, https://doi.org/10.1088/1742-6596/352/1/012009.

Pobrano z / Downloaded from Repository of Warsaw University of Technology 2025-09-24 11:16

[30] K.M. Dowling, H.S. Alpert, A.S. Yalamarthy, P.F. Satterthwaite, S. Kumar, H. Kock, U. Ausserlechner, D.G. Senesky, Micro-tesla offset in thermally stable AlGaN/GaN 2DEG Hall plates using current spinning, IEEE Sens. Lett. 3 (3) (2019) 1–4, https://doi.org/10.1109/lsens.2019.2898157.

[31] H.S. Alpert, C.A. Chapin, K.M. Dowling, S.R. Benbrook, H. Köck, U. Ausserlechner, D.G. Senesky, Sensitivity of 2DEG-based Hall-effect sensors at high temperatures, Rev. Sci. Instrum. 91 (2) (2020) 025003, https://doi.org/10.1063/1.5139911.

[32] N. Zurauskiene, V. Stankevic, S. Kersulis, J. Klimantavicius, C. Simkevicius, V. Plausinaitiene, M. Vagner, S. Balevicius, Increase of operating temperature of magnetic field sensors based on La–Sr–Mn–O films with mn excess, IEEE Trans. Plasma Sci. 47 (10) (2019) 4530–4535, https://doi.org/10.1109/tps.2019.2911545.

[33] T. Dalibor, G. Pensl, H. Matsunami, T. Kimoto, W.J. Choyke, A. Schöner, N. Nordell, Deep defect centers in silicon carbide monitored with deep level transient spectroscopy, Phys. Status Solidi A 162 (1) (1997) 199–225, https://doi.org/10.1002/1521-396X(199707)162:1<199::AID-PSSA199>3.0.CO;2-0, https://onlinelibrary.wiley.com/doi/pdf/10.1002/1521-396X%28199707%29162%3A1%3C199%3A%3AAID-PSSA199%3E3.0.CO%3B2-0.

[34] P. Kamiński, R. Kozłowski, M. Miczuga, M. Pawłowski, M. Kozubal, M. Pawłowski, High-resolution photoinduced transient spectroscopy of defect centers in vanadium-doped semi-insulating SiC, J. Mater. Sci., Mater. Electron. 19 (S1) (2008) 224–228, https://doi.org/10.1007/s10854-008-9576-6.

[35] P. Kamiński, R. Kozłowski, M. Miczuga, M. Pawłowski, M. Kozubal, J. Żelazko, Compensating defect centres in semi-insulating 6H-SiC, Opto-Electron. Rev. 17 (1) (2009) 1–7, https://doi.org/10.2478/s11772-008-0052-x.

[36] A. Dobrowolski, J. Jagiełło, K. Piętak-Jurczak, M. Wzorek, D. Czołak, T. Ciuk, Spectroscopic properties of close-to-perfect-monolayer quasi-free-standing epitaxial graphene on 6H-SiC(0001), Appl. Surf. Sci. (2023) 158617, https://doi.org/10.1016/j.apsusc.2023.158617.

[37] C. Berger, Z. Song, T. Li, X. Li, A.Y. Ogbazghi, R. Feng, Z. Dai, A.N. Marchenkov, E.H. Conrad, P.N. First, W.A. de Heer, Ultrathin epitaxial graphite: 2D electron gas properties and a route toward graphene-based nanoelectronics, J. Phys. Chem. B 108 (52) (2004) 19912–19916, https://doi.org/10.1021/jp040650f.

[38] J. Hass, W.A. de Heer, E.H. Conrad, The growth and morphology of epitaxial multilayer graphene, J. Phys. Condens. Matter 20 (32) (2008) 323202, https://doi.org/10.1088/0953-8984/20/32/323202.

[39] K.V. Emtsev, A. Bostwick, K. Horn, J. Jobst, G.L. Kellogg, L. Ley, J.L. McChesney, T. Ohta, S.A. Reshanov, J. Röhrl, E. Rotenberg, A.K. Schmid, D. Waldmann, H.B. Weber, T. Seyller, Towards wafer-size graphene layers by atmospheric pressure graphitization of silicon carbide, Nat. Mater. 8 (3) (2009) 203–207, https://doi.org/10.1038/nmat2382.

[40] S. Chen, M.H. von Hoegen, P.A. Thiel, M.C. Tringides, Diffraction paradox: an unusually broad diffraction background marks high quality graphene, Phys. Rev. B 100 (15) (Oct. 2019), https://doi.org/10.1103/physrevb.100.155307.

[41] J. Ristein, S. Mammadov, T. Seyller, Origin of doping in quasi-free-standing graphene on silicon carbide, Phys. Rev. Lett. 108 (24) (Jun. 2012), https://doi.org/10.1103/physrevlett.108.246104.

[42] S. Mammadov, J. Ristein, R.J. Koch, M. Ostler, C. Raidel, M. Wanke, R. Vasiliauskas, R. Yakimova, T. Seyller, Polarization doping of graphene on silicon carbide, 2D Mater. 1 (3) (2014) 035003, https://doi.org/10.1088/2053-1583/1/3/035003.

[43] J. Sławińska, H. Aramberri, M. Muñoz, J. Cerdá, Ab initio study of the relationship between spontaneous polarization and p-type doping in quasi-freestanding graphene on h-passivated SiC surfaces, Carbon 93 (2015) 88–104, https://doi.org/10.1016/j.carbon.2015.05.025.

[44] T. Ciuk, W. Strupinski, Statistics of epitaxial graphene for Hall effect sensors, Carbon 93 (2015) 1042–1049, https://doi.org/10.1016/j.carbon.2015.06.032.

[45] T. Ciuk, P. Caban, W. Strupinski, Charge carrier concentration and offset voltage in quasi-free-standing monolayer chemical vapor deposition graphene on SiC, Carbon 101 (2016) 431–438, https://doi.org/10.1016/j.carbon.2016.01.093.

[46] T. Ciuk, O. Petruk, A. Kowalik, I. Jozwik, A. Rychter, J. Szmidt, W. Strupinski, Low-noise epitaxial graphene on SiC Hall effect element for commercial applications, Appl. Phys. Lett. 108 (22) (2016) 223504, https://doi.org/10.1063/1.4953258.

[47] S. Sridhara, T. Eperjesi, R. Devaty, W. Choyke, Penetration depths in the ultraviolet for 4H, 6H and 3C silicon carbide at seven common laser pumping wavelengths, Mater. Sci. Eng. B 61–62 (1999) 229–233, https://doi.org/10.1016/s0921-5107(98)00508-x.

[48] N. Watanabe, T. Kimoto, J. Suda, Temperature dependence of optical absorption coefficient of 4H- and 6H-SiC from room temperature to 300 °C, Jpn. J. Appl. Phys. 53 (10) (2014) 108003, https://doi.org/10.7567/jjap.53.108003.

[49] D.M. Caughey, R.E. Thomas, Carrier mobilities in silicon empirically related to doping and field, Proc. IEEE 55 (12) (1967) 2192–2193.

[50] W.J. Schaffer, G.H. Negley, K.G. Irvine, J.W. Palmour, Conductivity anisotropy in epitaxial 6H and 4H Sic, MRS Proc. 339 (1994), https://doi.org/10.1557/proc-339-595.

[51] M. Roschke, F. Schwierz, Electron mobility models for 4H, 6H, and 3C SiC [MESFETs], IEEE Trans. Electron Devices 48 (7) (2001) 1442–1447.

[52] K. Momma, F. Izumi, *VESTA 3* for three-dimensional visualization of crystal, volumetric and morphology data, J. Appl. Crystallogr. 44 (6) (2011) 1272–1276, https://doi.org/10.1107/s0021889811038970.

[53] L.S. Ramsdell, J.A. Kohn, Developments in silicon carbide research, Acta Crystallogr. 5 (2) (1952) 215–224, https://doi.org/10.1107/s0365110x52000617.

[54] A. Merkys, A. Vaitkus, A. Grybauskas, A. Konovalovas, M. Quirós, S. Gražulis, Graph isomorphism-based algorithm for cross-checking chemical and crystallographic descriptions, J. Cheminform. 15 (1) (Feb. 2023), https://doi.org/10.1186/s13321-023-00692-1.

[55] A. Vaitkus, A. Merkys, S. Gražulis, Validation of the crystallography open database using the crystallographic information framework, J. Appl. Crystallogr. 54 (2) (2021) 661–672, https://doi.org/10.1107/s1600576720016532.

[56] M. Quirós, S. Gražulis, S. Girdzijauskaitė, A. Merkys, A. Vaitkus, Using SMILES strings for the description of chemical connectivity in the crystallography open database, J. Cheminform. 10 (1) (May 2018), https://doi.org/10.1186/s13321-018-0279-6.

[57] A. Merkys, A. Vaitkus, J. Butkus, M. Okulič-Kazarinas, V. Kairys, S. Gražulis, *COD::CIF::parser*: an error-correcting CIF parser for the Perl language, J. Appl. Crystallogr. 49 (1) (2016) 292–301, https://doi.org/10.1107/s1600576715022396.

[58] S. Gražulis, A. Merkys, A. Vaitkus, M. Okulič-Kazarinas, Computing stoichiometric molecular composition from crystal structures, J. Appl. Crystallogr. 48 (1) (2015) 85–91, https://doi.org/10.1107/s1600576714025904.

[59] S. Gražulis, D. Chateigner, R.T. Downs, A.F.T. Yokochi, M. Quirós, L. Lutterotti, E. Manakova, J. Butkus, P. Moeck, A.L. Bail, Crystallography open database – an open-access collection of crystal structures, J. Appl. Crystallogr. 42 (4) (2009) 726–729, https://doi.org/10.1107/s0021889809016690.

[60] S. Gražulis, A. Daškevič, A. Merkys, D. Chateigner, L. Lutterotti, M. Quirós, N.R. Serebryanaya, P. Moeck, R.T. Downs, A.L. Bail, Crystallography open database (COD): an open-access collection of crystal structures and platform for world-wide collaboration, Nucleic Acids Res. 40 (D1) (2011) D420–D427, https://doi.org/10.1093/nar/gkr900.

[61] R.T. Downs, M. Hall-Wallace, The American mineralogist crystal structure database, Am. Mineral. 88 (2003) 247–250.

[62] Y. Goldberg, M.E. Levinshtein, S.L. Rumyantsev, in: M.E. Levinshtein, S.L. Rumyantsev, M.S. Shur (Eds.), Properties of Advanced Semiconductor Materials GaN, AlN, SiC, BN, SiC, SiGe, John Wiley & Sons, 2001.

[63] A. Dobrowolski, J. Jagiełło, D. Czołak, T. Ciuk, Determining the number of graphene layers based on Raman response of the SiC substrate, Physica E, Low-Dimens. Syst. Nanostruct. 134 (2021) 114853, https://doi.org/10.1016/j.physe.2021.114853.

[64] K. Piętak, J. Jagiełło, A. Dobrowolski, R. Budzich, A. Wysmołek, T. Ciuk, Enhancement of graphene-related and substrate-related Raman modes through dielectric layer deposition, Appl. Phys. Lett. 120 (6) (2022) 063105, https://doi.org/10.1063/5.0082694.

[65] M. Pawłowski, P. Kamiński, R. Kozłowski, S. Jankowski, M. Wierzbowski, Intelligent measuring system for characterisation of defect centres in semi-insulating materials by photoinduced transient spectroscopy, Metrol. Meas. Syst. 12 (2) (2005) 207–228.

[66] L. Storasta, J.P. Bergman, E. Janzén, A. Henry, J. Lu, Deep levels created by low energy electron irradiation in 4H-SiC, J. Appl. Phys. 96 (9) (2004) 4909–4915, https://doi.org/10.1063/1.1778819.

[67] M. Gong, S. Fung, C.D. Beling, Z. You, Electron-irradiation-induced deep levels in *n*-type 6H–SiC, J. Appl. Phys. 85 (11) (1999) 7604–7608, https://doi.org/10.1063/1.370561.

[68] M. Pavesi, M. Manfredi, P.L. Rigolli, N. Armani, G. Salviati, Optical characterization of radiative deep centres in 6H–SiC junction field effect transistors, Semicond. Sci. Technol. 19 (1) (2003) 45, https://doi.org/10.1088/0268-1242/19/1/007.

[69] T. Troffer, M. Schadt, T. Frank, H. Itoh, G. Pensl, J. Heindl, H.P. Strunk, M. Maier, Doping of SiC by implantation of boron and aluminum, Phys. Status Solidi A 162 (1) (1997) 277–298, https://doi.org/10.1002/1521-396X(199707)162:1<277::AID-PSSA277>3.0.CO;2-C, https://onlinelibrary.wiley.com/doi/pdf/10.1002/1521-396X%28199707%29162%3A1%3C277%3A%3AAID-PSSA277%3E3.0.CO%3B2-C.

[70] G. Alfieri, E. Monakhov, B. Svensson, A. Hallén, Defect energy levels in hydrogen-implanted and electron-irradiated n-type 4H silicon carbide, J. Appl. Phys. 98 (2005) 113524, https://doi.org/10.1063/1.2139831.

[71] M.E. Bathen, L. Vines, Manipulating single-photon emission from point defects in diamond and silicon carbide, Adv. Quantum Technol. 4 (7) (2021) 2100003, https://doi.org/10.1002/qute.202100003.

[72] A. Castaldini, A. Cavallini, L. Rigutti, F. Nava, S. Ferrero, F. Giorgis, Deep levels by proton and electron irradiation in 4H–SiC, J. Appl. Phys. 98 (5) (2005) 053706, https://doi.org/10.1063/1.2014941.

[73] D. Davydov, A. Lebedev, V. Kozlovski, N. Savkina, A. Strel'chuk, DLTS study of defects in 6H- and 4H-SiC created by proton irradiation, Physica B, Condens. Matter 308–310 (2001) 641–644, https://doi.org/10.1016/s0921-4526(01)00775-x.

[74] M.E. Bathen, C.T.-K. Lew, J. Woerle, C. Dorfer, U. Grossner, S. Castelletto, B.C. Johnson, Characterization methods for defects and devices in silicon carbide, J. Appl. Phys. 131 (14) (2022) 140903, https://doi.org/10.1063/5.0077299.